Experimental investigation of phase relations in the system NaAlSi$_3$O$_8$–H$_2$O at high temperatures and pressures: liquidus relations, liquid–vapor mixing, and critical phenomena at deep crust–upper mantle conditions

Adam R. Makhluf[1] · R. C. Newton[1] · C. E. Manning[1]

Abstract

Supercritical fluids in rock–H$_2$O systems have been proposed to be important agents of mass transfer in subduction zone environments. New experimental studies were conducted on the simple model granite system NaAlSi$_3$O$_8$ (Ab)–H$_2$O in order to investigate phase relations and to develop the thermodynamic mixing properties between aqueous fluid (a.k.a. vapor, V) and silicate melt (a.k.a. liquid, L) at pressures (P) and temperatures (T) approaching those of critical mixing. We established liquidus and solvus phase relations by analyzing the quenched run products from piston–cylinder experiments over a range of $P - T - X_{\mathrm{H_2O}}$ conditions from 1.0 to 1.7 GPa, 630–1060 °C and 4–92 wt% H$_2$O. Equations for the critical curve, solidus temperatures, albite solubility at the solidus, and vapor-saturated solidus H$_2$O content were formulated as functions of $P - T - X_{\mathrm{H_2O}}$. We constructed a subregular solution model to describe the solvus curves using P and T dependent Margules coefficients ($W_{\mathrm{H_2O}}$ and W_{Ab}). Activities of H$_2$O and Ab ($a_{\mathrm{H_2O}}$ and a_{Ab}) could be formulated using only the input at the solidus and the critical point at each pressure because of the nearly linear dependence of the parameters on T. The solvus curves were confirmed independently by means of criteria established for classification of quenched products as L, $L+V$, or V and are in excellent agreement with the compositions that can be calculated using the Margules coefficients. At 1.6 GPa, the H$_2$O content at the vapor-saturated solidus is 44.5 ± 5.5 wt% and the solubility of albite at the solidus is 42.95 ± 0.99 wt%, indicating the imminent intersection of the two curves and thus a stable critical endpoint at some slightly higher pressure. We constrain the critical endpoint at 1.63 ± 0.02 GPa, 659 ± 5 °C, and a composition of ~ 44.7 wt% H$_2$O based on the intersections of the pressure dependent solidus curves with the critical curve, the pressure dependent albite solubility curve with the vapor-saturated solidus curve. The 1.7 GPa experiments showed no evidence for liquid–vapor immiscibility across a wide range of compositions and temperatures (4–80 wt% H$_2$O and 630–1050 °C, and furthermore, that low albite is stable in the presence of the supercritical fluid near the breakdown of albite to jadeite and quartz. These results provide a comprehensive account of the solution properties of subcritical and supercritical fluids in this model granite system at temperatures and pressures corresponding to the deep-crust regions of granite magma generation.

Keywords Albite · Water · Supercritical fluid · Liquidus · Solubility · Immiscibility · Hydrous melting · Granite

Communicated by Mark S Ghiorso.

✉ Adam R. Makhluf
amakhluf@epss.ucla.edu

1   Department of Earth, Planetary and Space Sciences, University of California, Los Angeles, 595 Charles E. Young Drive, East, 1679 Geology Building, Los Angeles, CA 90095-1567, USA

Introduction

Water plays an important role in the production and properties of silicate magmas in Earth's crust and mantle. Key to water's influence is the strong pressure dependence of solubility: as P increases at water saturation, the amount of H$_2$O dissolved in a coexisting silicate liquid increases (e.g., Manning 2018 and references therein). At sufficiently high pressure, silicate liquids, and H$_2$O become completely miscible, such that a single fluid phase is stable across the

entire compositional range from crystal saturation to pure H_2O. The $P–T$ trace of transition to a supercritical fluid, termed the critical curve, occurs at progressively lower T with increasing pressure. The intersection of the critical curve and the solidus, or second critical endpoint, terminates the solidus; at pressures higher than the endpoint, the solidus is replaced by a continuous solubility field. It appears that, for many model and natural silicate systems, a critical curve intersects the solidus at lower-crustal to upper-mantle pressures (Bureau and Keppler 1999; Hermann et al. 2006), and there is evidence that sediment–H_2O systems at the top of subducting slabs attain $P–T$ conditions near the critical endpoint on the melting curve (e.g., Cooper et al. 2012).

Characterization of phase relations in the $P–T$ vicinity of the second critical endpoint is challenging. Numerous methods have been employed, including interpretation of quench textures (Boettcher and Wyllie 1969; Makhluf et al. 2016) measurement of mineral solubility (Hunt and Manning 2012; Kennedy et al. 1962; Newton and Manning 2008; Nowak and Behrens 1995; Stalder et al. 2000, 2001; Stolper 1989), spectroscopic analysis of hydrous glasses, compositional trends or solubility trends of minor and trace components (Hayden and Manning 2011; Hermann and Spandler 2007; Kessel et al. 2005) and direct imaging approaches using hydrothermal diamond–anvil cells (Bureau and Keppler 1999; Shen and Keppler 1997) and X-ray radiography (Kawamoto et al. 2012; Mibe et al. 2004, 2007, 2011). The proliferation of techniques has led to conflicting determinations of the locations of second critical endpoints. For example, the second critical endpoint on the hydrous basalt melting curve has been proposed to lie at 5.5 ± 0.5 GPa and 1050 ± 50 °C by Kessel et al. (2005), but at 3.4 GPa and 770 °C by Mibe et al. (2011). Discrepancies are even larger in the peridotite–H_2O system (Grove et al. 2006, 2012; Mibe et al. 2007; Till et al. 2012). Even in simple silicate–H_2O systems like $NaAlSi_3O_8$ (albite)–H_2O, phase relations at near-critical $P–T$ conditions remain uncertain. Unlike SiO_2 (quartz)–H_2O, where phase relations are well established (Hunt and Manning 2012; Kennedy et al. 1962; Nakamura 1974; Newton and Manning 2008), additional experimental observations of critical phenomena in the much-studied albite–H_2O system are needed to clarify such features as the $P–T$ conditions of a critical endpoint on the hydrous melting curve of albite, and the compositions of critical fluids.

Early investigations of $NaAlSi_3O_8$–H_2O at $P > 1$ GPa did not identify a role for critical mixing near the hydrous melting curve. Boettcher and Wyllie found evidence for a transition from congruent melting ($Ab + V = L$) to incongruent melting to jadeite ($NaAlSi_2O_6$) plus liquid ($Ab + V = L + Jd$) at about 1.6 GPa and 700 °C. Their interpretation of experiments on $NaAlSi_3O_8$–H_2O melting to pressures above 2.5 GPa invoked subcritical melting. Neither Eggler and Kadik (1979) nor Goldsmith and Jenkins

(1985b) envisioned critical phenomena in the binary system at high pressures, although the latter authors observed major textural changes in quenched charges in melting experiments near 1.7 GPa, from the bubbly glass formed in lower P experiments to a friable, frothy substance that they pointedly refrained from calling a glass, but used the term "quenched fluid" instead.

Attempts to estimate the H_2O contents of melts in the binary system were based on the measurements at lower pressures on bubble-free quenched glasses, guided by volumetric measurements in hydrous melts (McMillan and Holloway 1987) and/or theoretical models of H_2O speciation (Burnham 1975; Silver and Stolper 1985). These extrapolations have been useful in explaining the great increase in the H_2O solubility in albite melts with pressure, but all suggested that increasing T at constant P should cause decrease in the solubility.

The ion microprobe measurements of Paillat et al. (1992) on H_2O contents from vapor-saturated melting experiments in the system $NaAlSi_3O_8$–H_2O at 0.5–1.3 GPa and super-solidus temperatures above 900 °C created a new paradigm. Their measurements clearly showed that, at pressures above 0.5 GPa, the H_2O solubility is "prograde"; that is, it increases with increasing T at constant pressure. They noted that this implies that, at some elevated P and T, critical mixing of H_2O-rich silicate melt and $NaAlSi_3O_8$-rich aqueous fluid must occur. This prediction was confirmed by Shen and Keppler (1997), who optically observed merging of two discrete fluids (melt and vapor) with increasing P and T in a diamond–anvil cell. Paillat et al. (1992) noted that the transition to incongruent hydrous melting of albite observed by Boettcher and Wyllie (1969) (their "singular point") could also plausibly be explained as a critical endpoint on the hydrous melting curve of albite near 1.6 GPa and 670 °C, a conclusion reached by both Stalder et al. (2000) and Kawamoto et al. (2012), and modeled based on the low-pressure experimental data by Zeng and Nekvasil (1996).

Behrens (1995) measured H_2O contents of the fluid–$NaAlSi_3O_8$–H_2O glass quenched from experiments at 1100 °C and pressures up to 0.5 GPa, using several different analysis techniques. He found lower H_2O solubilities than found by previous studies at the same $P–T$ conditions, including those of Paillat et al. (1992), and apparent dependence of the solubility on the ratio of fluid phase to melt phase in the experiments. These experiments illustrate the difficulty of determination of equilibrium H_2O by analysis of quenched hydrous glasses, especially in view of the much higher solubilities to be encountered at higher H_2O pressure. Gavrilenko et al. (2019) found that no more than about 9 wt% H_2O could be quenched into glasses of andesitic composition in piston–cylinder experiments. This quantity is much smaller than estimated for near-critical magma–H_2O systems. Determination of compositions of

near-critical silicate–H_2O systems by chemical analysis of quenched material is clearly impossible.

The experiments of the present study were designed to address these issues by characterizing as precisely as possible the phases and textures returned by quenching of experiments at higher pressure on melting in the albite–H_2O system. This method was used successfully by Burnham and Jahns (1962) to measure liquidus and solidus temperatures and compositions at elevated pressures in this system. We combined this technique with precise solubility measurements of albite in H_2O at near solidus conditions to define, at five different pressures in the range 1–1.7 GPa (1) the liquidus surfaces, (2) $T - X_{H_2O}$ relations at vapor saturation (the solvus), (3) the near-solidus solubility of albite, and (4) the temperature and composition of critical mixing of liquid and vapor. The results lead to an improved characterization of the $P - T - X_{H_2O}$ phase relations near the second critical endpoint, a precise determination of the liquidus surface, and a thermodynamic model of $NaAlSi_3O_8$–H_2O mixing to describe fluid compositions and critical phenomena. This model may serve as a guide to expected behavior of more complex water–rock systems at high P and T, and could help to discriminate among competing interpretations of the diagrams in more complex systems emulating natural rocks.

Experimental and analytical methods

Starting materials and sample loading

Starting materials were a well characterized low albite from Amelia County (Virginia, USA) and ultrapure water (~ 18 MΩ cm^2/cm resistivity). Chemical analyses and X-ray diffraction (XRD) data confirming the purity and low structural state are given in Makhluf et al. (2016). The albite was prepared for experiments by grinding under acetone in an agate mortar for ~ 30 min until complete evaporation and then drying in an oven at 600 °C for ~ 30 min to volatilize any organic residue.

Pt tubing segments of ~ 1.25–1.75 cm length and 2 mm or 3.5 mm outer diameter were cleaned with acetone. Wall thickness of the 2 mm tubing was 0.13 mm and the that of the 3.5 mm tubing was 0.25 mm. The larger capsules were used in experiments that had very small mole fractions of water, as well as for solubility experiments where large amounts of both albite and water were needed. One side of the tube was sealed in an oxygen–acetylene flame and then the whole capsule was annealed with this flame. Weighed amounts of albite and water were loaded into the capsules then sealed by arc-welding. Amounts of total charge were 10–40 mg. Water mole fractions ranged from 0.035 to 0.99. Sealed capsules were weighed to check for H_2O loss. Weight losses were typically less than about 200 μg, which

corresponds to the typical Pt evaporation mass as established by welding and reweighing dry capsules. All weighings were carried out on a Mettler Toledo UMX2 ultra-microbalance with a stated precision of 2×10^{-4} mg.

Piston–cylinder methods

Experiments were conducted in a piston–cylinder apparatus of either 2.54 or 1.91 cm diameter using methods similar to those in Makhluf et al. (2016) Furnaces employed graphite sleeves immersed in a NaCl pressure medium. Temperature was digitally measured and controlled using S-type thermocouples, with an uncertainty of ± 3 °C. Pressure uncertainty was ± 30 MPa. No correction was made for the effect of pressure on thermocouple emf. Experiments were held at desired P and T for varying times, depending on the T and H_2O content. Experiments at temperatures higher than 900 °C required the use of small (0.15 inch length) BN inserts placed above and below the capsule to prevent melting of the pressure medium. BN powder was packed around capsules in these high-T runs. The BN–NaCl pressure medium required a pressure correction of -60 MPa relative to the NaCl pressure medium, determined using quartz solubility experiments previously performed in our lab (Manning 1994) in NaCl-only pressure media.

After each experiment, we verified the integrity of the capsules by reweighing each capsule to check for H_2O loss. Any capsule that lost weight was discounted. No detectable weight loss of quenched capsules was observed even for experiments at the highest T of 1060 °C, consistent with the expectation that temperatures were lower than those at which H_2O can be lost by diffusion through Pt capsules (Truckenbrodt and Johannes 1999). This method defines bulk H_2O of each experiment without recourse to analytical methods, for which accuracy may be problematic because of calibration uncertainties (e.g., Bartoli et al. 2016) and vesiculation of water during quenching (Gavrilenko et al. 2019).

Solubility measurements

Albite solubility measurements were conducted in order to constrain the isobaric-invariant composition of the H_2O-rich limb of the solvus at the solidus. Following methods of Newton and Manning (2008) and Makhluf et al. (2016), measurements were made at temperatures 5–10 °C below the vapor-saturated solidus at each pressure. Manning et al. (2010) showed the importance of making this measurement as close to the solidus temperature as possible due to substantial increase in mineral solubility as the solidus temperate is approached from below (see their Fig. 2a). The determination of the solidus temperatures of low albite with H_2O by Goldsmith and Jenkins (1985b) was used as an initial guide for conducting these experiments.

For the solubility experiments, we used albite ground to ~ 100–600 μm diameter instead of polished single crystals because, in preliminary experiments, polished single crystals fragmented into many small pieces along deep solution channels that followed fractures and/or cleavage planes. Fragmentation was exacerbated by the high solubility of albite, especially at the higher pressures in the range investigated. The experiments bracket a solubility value by inspection of the charge for the presence or absence of crystals after the run using a petrographic microscope.

Demonstration of equilibrium

Experimental times were generally < 24 h at T < 1000 °C, 2–7 h at $T \geq 1000$ °C and up to 2 weeks for temperatures near the solidus (700 °C and lower). Runs were quenched to < 200 °C in ~ 30 s. Repeat experiments were made to assure time independence of the measurements at several P–T conditions. Several two-step reversal experiments along the liquidus were made that were initially brought to a high T to melt the sample completely, followed by a temperature drop for attempted crystallization of the charges. The temperature was held at the higher T for at least 4 h and > 24 h at the lower T. The pressure was restored during the temperature drop.

Analytical methods for run products

All run products were characterized by analysis with a petrographic microscope of either polished thick sections or by immersion oil mounts of granular material. Phase relations involving hydrous albite liquid, H_2O-rich vapor or supercritical fluid were determined from textural analysis of run products (see below for details) by binocular, petrographic, and scanning electron microscopy (SEM). While the results in some experiments were easily interpreted using binocular and petrographic microscope techniques, other samples required characterization by SEM, especially those quenched from near-critical conditions. For SEM analysis, we used a Tescan Vega-3 XMU SEM with both secondary and backscattered electrons. A PANalytic powder diffractometer was used to check for crystalline phases in selected near-liquidus and subsolidus runs; scans were conducted in the range $20° < 2\theta < 60°$ at ~ 2° min^{-1} with Cu Kα radiation of wavelength 1.5406 Å. The diffractometer was calibrated against the (111) peak of a high purity silicon wafer.

Results of experiments

Interpretation of run products

The results of experiments are presented in Tables 1 and 2. Criteria for assigning run products to each stability field are given below. We built upon methods of Makhluf et al. (2016) for classifying run products by extending them to include quenched supercritical fluids. Interpretations of the run products were made, and are described below, with reference to $T - X_{H_2O}$ phase relations at pressures below a second critical endpoint on the vapor-saturated solidus (Fig. 1). This textural framework also aids in identifying conditions at pressures higher than the second critical endpoint.

Liquid + albite field

We used the dry melting temperatures of albite from Boyd and England (1963) at each of the pressures to define the initial point on the hydrous melting curves. Quenched run products assigned to the liquid + albite field reveal varying amounts of crystals and glass depending on $P - T - X_{H_2O}$ conditions. A typical quenched run product (Fig. 2a) shows albite embedded in a glass matrix. The albite typically displayed subhedral crystal habit and polysynthetic twinning. H_2O exsolved from the liquid phase during quenching formed bubbles trapped in the glass when X_{H_2O} in the coexisting liquid was greater that approximately 8 wt%.

Liquid field

The liquid field in isobaric $T - X_{H_2O}$ sections is bounded at low H_2O by coexistence with crystals, and at high H_2O by coexistence with an aqueous vapor. The absence of a phase boundary marking coexistence with aqueous vapor at high H_2O indicates an experiment is in the supercritical field (see below). Quenched run products assigned to the liquid field were characterized by a crystal-free glass with varying abundance of bubbles interpreted to result from H_2O exsolution on quenching (Fig. 2b, c). Bubble density and size in quenched glasses increase with increasing bulk H_2O content at a fixed P and temperature.

Miscibility gap

A silicate-rich liquid phase and a H_2O-rich vapor phase coexist in bulk compositions lying within the miscibility gap, or solvus. Quench textures in experiments interpreted to reflect coexisting liquid and vapor vary with bulk H_2O content. Run products from compositions at low H_2O inside of the solvus contains clear glass balls representing a quenched vapor phase that occur in cavities, interpreted as former vapor pockets, near the pinched end of the capsule. Figure 2d shows a typical example of a quenched charge that was run at a temperature close to the vapor-saturated solidus. The vapor-precipitated glass balls are either devoid of bubbles or have clear rims with a few bubbles in the center, and are quite distinct from the bubbly glass shards in samples that are interpreted to represent the former liquid phase. This

Table 1 Results of experiments of albite in H_2O from 1.0 to 1.7 GPa and 650 to 1060 °C

Run	P (GPa)	T (°C)	H_2O (wt%)	Time (h)	Run products
Ab09	1.00	700	16.79	68	*L* + Albite
Ab05	1.00	750	10.93	24	*L* + Albite
Ab08	1.00	750	11.72	22	*L* + Albite
Ab01	1.00	800	8.79	50	*L* + Albite
Ab02	1.00	800	4.06	50	*L* + Albite
Ab07	1.00	800	10.11	24	*L* + Albite
Ab23R	1.00	800	8.01	46	*L* + Albite
Ab11	1.00	850	6.44	23	*L* + Albite
Ab15	1.00	850	7.23	24	*L* + Albite
Ab236R	1.00	850	7.24	27	*L* + Albite
Ab16	1.00	900	6.61	23	*L* + Albite
Ab234R	1.00	900	6.57	42	*L* + Albite
Ab79	1.00	950	4.99	67	*L* + Albite
Ab258	1.00	1050	3.08	20	*L* + Albite
Ab24	1.00	700	18.02	64	*L*
Ab06	1.00	750	12.56	19	*L*
Ab18	1.00	750	20.00	88	*L*
Ab32	1.00	750	20.00	51	*L*
Ab31	1.00	750	21.72	51	*L*
Ab04	1.00	800	11.40	24	*L*
Ab03	1.00	800	13.35	24	*L*
Ab26	1.00	800	22.94	68	*L*
Ab237R	1.00	850	8.73	27	*L*
Ab39	1.00	850	23.95	26	*L*
Ab40	1.00	850	25.72	26	*L*
Ab235R	1.00	900	7.95	42	*L*
Ab78	1.00	950	6.49	67	*L*
Ab259	1.00	1050	4.14	20	*L*
Ab25	1.00	700	19.48	64	*L* + *V*
Ab231	1.00	700	22.55	93	*L* + *V*
Ab19	1.00	700	46.92	75	*L* + *V*
Ab20	1.00	750	23.07	68	*L* + *V*
Ab21	1.00	750	35.02	68	*L* + *V*
Ab22	1.00	750	75.07	72	*L* + *V*
Ab44	1.00	750	86.09	74	*L* + *V*
Ab27	1.00	800	26.13	68	*L* + *V*
Ab41	1.00	800	81.96	44	*L* + *V*
Ab29	1.00	850	27.99	23	*L* + *V*
Ab30	1.00	850	30.24	23	*L* + *V*
Ab38	1.00	850	79.94	23	*L* + *V*
Ab46	1.00	900	26.05	19.5	*L* + *V*
Ab57	1.00	950	27.60	2	*L* + *V*
Ab45	1.00	900	29.69	19.5	*L* + *V*
Ab35	1.00	900	74.08	21	*L* + *V*
Ab42	1.00	900	78.21	50	*L* + *V*
Ab53	1.00	950	31.08	2	*L* + *V*
Ab49	1.00	950	32.58	22	*L* + *V*
Ab50	1.00	950	33.41	3	*L* + *V*
Ab56	1.00	950	50.45	3	*L* + *V*
Ab58	1.00	950	67.65	1	*L* + *V*
Ab43	1.00	950	68.21	72	*L* + *V*

Table 1 (continued)

Run	P (GPa)	T (°C)	H_2O (wt%)	Time (h)	Run products
Ab47	1.00	950	71.33	22	$L+V$
Ab48	1.00	950	73.86	22	$L+V$
Ab60	1.00	970	40.24	2	$L+V$
Ab66	1.00	980	59.68	3	$L+V$
Ab59	1.00	990	39.91	2	$L+V$
Ab62	1.00	1000	50.27	2	$L+V$
Ab61	1.00	1010	28.57	2	$L+V$
Ab63	1.00	1035	50.00	2	$L+V$
Ab71	1.00	1035	50.05	21	$L+V$
Ab67	1.00	1040	40.17	7	$L+V$
Ab34	1.00	750	87.87	47	V
Ab37	1.00	800	84.89	24	V
Ab33	1.00	850	83.22	23	V
Ab76	1.00	900	78.00	22	V
Ab28	1.00	900	80.02	21	V
Ab55	1.00	950	71.50	2	V
Ab54	1.00	950	74.52	3	V
Ab51	1.00	950	77.46	3	V
Ab52	1.00	950	79.94	3	V
Ab65	1.00	1020	60.16	4	V
Ab72	1.00	1060	39.84	26	SCF
Ab64	1.00	1060	50.10	3	SCF
Ab70	1.00	1060	50.36	7	SCF
Ab69	1.00	1060	60.02	7	SCF
Ab93	1.25	700	17.54	117	$L+$Albite
Ab81	1.25	800	10.53	22.5	$L+$Albite
Ab99	1.25	900	6.57	70	$L+$Albite
Ab88	1.25	700	20.24	69	L
Ab90	1.25	800	12.76	70	L
Ab80	1.25	800	18.27	22.5	L
Ab227	1.25	850	25.08	24	L
Ab95	1.25	900	8.05	22	L
Ab96	1.25	900	11.18	22	L
Ab226	1.25	700	25.39	117	$L+V$
Ab89	1.25	700	31.22	69	$L+V$
Ab104	1.25	700	33.20	94	$L+V$
Ab105	1.25	700	37.29	94	$L+V$
Ab94	1.25	700	40.31	117	$L+V$
Ab111	1.25	700	64.99	42	$L+V$
Ab106	1.25	700	69.94	22	$L+V$
Ab116	1.25	700	70.72	96	$L+V$
Ab181	1.25	775	61.77	168	$L+V$
Ab91	1.25	800	30.93	70	$L+V$
Ab113	1.25	800	37.68	40	$L+V$
Ab175	1.25	800	37.87	10	$L+V$
Ab179	1.25	800	41.14	44	$L+V$
Ab112	1.25	800	42.21	40	$L+V$
Ab107	1.25	800	48.96	21	$L+V$
Ab125	1.25	800	56.14	96	$L+V$
Ab130	1.25	800	58.97	116	$L+V$
Ab119	1.25	800	60.14	91	$L+V$

Table 1 (continued)

Run	P (GPa)	T (°C)	H₂O (wt%)	Time (h)	Run products
Ab131	1.25	850	45.39	70	L+V
Ab114	1.25	850	48.64	28	L+V
Ab132	1.25	850	55.03	70	L+V
Ab136	1.25	870	52.17	73	L+V
Ab121	1.25	875	49.07	24	L+V
Ab129	1.25	880	44.16	50	L+V
Ab100	1.25	900	48.97	70	L+V
Ab194	1.25	920	45.14	16	L+V
Ab177	1.25	700	70.62	118	V
Ab178	1.25	700	73.21	118	V
Ab124	1.25	700	73.37	72	V
Ab110	1.25	700	75.84	46	V
Ab189	1.25	700	79.98	60	V
Ab182	1.25	775	69.66	168	V
Ab115	1.25	800	62.73	23	V
Ab128	1.25	880	55.36	50	V
Ab198	1.25	960	38.22	3	SCF
Ab165	1.25	920	50.01	71	SCF
Ab197	1.25	960	50.06	3	SCF
Ab143	1.40	700	19.52	92	L+Albite
Ab135	1.40	700	22.59	118	L+Albite
Ab146	1.40	800	11.44	45	L+Albite
Ab148	1.40	900	7.26	25	L+Albite
Ab233	1.40	700	29.63	23	L
Ab147	1.40	800	13.51	45	L
Ab232	1.40	800	32.22	24	L
Ab149	1.40	900	9.12	25	L
Ab228	1.40	700	32.12	24	L+V
Ab144	1.40	700	43.67	92	L+V
Ab150	1.40	700	57.83	65	L+V
Ab191	1.40	750	46.02	24	L+V
Ab126	1.40	750	48.99	72	L+V
Ab156	1.40	750	53.35	96	L+V
Ab224	1.40	800	41.02	24	L+V
Ab192	1.40	800	45.05	176	L+V
Ab127	1.40	800	49.37	69	L+V
Ab164	1.40	815	49.62	66	L+V
Ab142	1.40	700	60.97	99	V
Ab196	1.40	700	70.08	199	V
Ab190	1.40	750	64.09	24	V
Ab157	1.40	750	57.00	96	V
Ab193	1.40	800	54.35	176	V
Ab133	1.40	830	50.19	98	SCF or V
Ab218	1.40	860	45.22	42	SCF
Ab230	1.60	670	30.62	29	L+Albite
Ab159	1.60	700	21.89	81	L+Albite
Ab158	1.60	800	11.88	20	L+Albite
Ab155	1.60	900	7.34	24	L+Albite
Ab229	1.60	670	39.06	68	L
Ab160	1.60	700	25.22	81	L
Ab153	1.60	800	14.10	23	L

Table 1 (continued)

Run	P (GPa)	T (°C)	H₂O (wt%)	Time (h)	Run products
Ab151	1.60	900	9.03	18	*L*
Ab140	1.60	690	49.90	68	SCF or *L* + *V*
Ab166	1.60	680	50.01	191	SCF or *L* + *V*
Ab139	1.60	690	51.47	49	SCF
Ab122	1.60	700	58.06	77	SCF
Ab173	1.60	710	49.98	115	SCF
Ab206	1.70	630	65.26	20	SCF + Albite
Ab205	1.70	630	79.72	20	SCF + Albite
Ab163	1.70	650	35.31	69	SCF + Albite
Ab214	1.70	650	49.88	99	SCF + Albite
Ab162	1.70	650	49.97	69	SCF + Albite
Ab215	1.70	650	63.78	99	SCF + Albite
Ab210	1.70	675	32.74	16	SCF + Albite
Ab211	1.70	720	19.54	77	SCF + Albite
Ab170	1.70	800	12.48	75	SCF + Albite
Ab169	1.70	900	8.21	74	SCF + Albite
Ab221	1.70	1050	4.43	44	SCF + Albite
Ab204	1.70	650	80.12	41	SCF
Ab172	1.70	665	50.01	141	SCF
Ab222	1.70	665	64.96	94	SCF
Ab202	1.70	700	33.80	41	SCF
Ab207	1.70	740	19.97	24	SCF
Ab171	1.70	800	13.50	75	SCF
Ab168	1.70	900	8.95	74	SCF
Ab220	1.70	1050	6.40	44	SCF

See Table 2 for results of subsolidus albite solubility experiments

L quenched liquid, *V* quenched vapor, *SCF* quenched supercritical fluid. Uncertainties: average standard error in weighings are 0.4 μg, pressure and temperature are within 0.03 GPa and 3 °C

Italicized run numbers at 1 GPa indicate results from Makhluf et al. (2016). Run numbers appended with "R" are reversal experiments which were initially equilibrated at *T* in liquid field before cooling to listed *T* for listed time (see Makhluf et al. 2016)

criterion was used by Burnham and Jahns (1962) to infer the existence of a separate aqueous fluid (vapor) phase coexisting with a silicate melt (liquid).

As bulk H₂O concentration increases within the miscibility gap, the quenched hydrous glass occupies progressively less of the capsule until, at high H₂O, run products display spheroidal masses of hydrous glass coexisting with myriad small spherules (Fig. 2e). This textural evolution is consistent with vapor concentration becoming large enough that the liquid is surrounded by the vapor phase, and surface tension causes the liquid to collect into pools. The large spheroids of quenched glass are opaque, white, and porcelaneous when viewed with the unaided eye or with a binocular microscope. High density of tiny bubbles in the spheroids causes strong light scattering; this color and texture further distinguish the quenched liquid phase from quenched solute spherules.

With increasing temperature, the liquid and vapor approach each other in composition and physical properties, so that textures in the quenched charges become harder to interpret. Near the critical temperature, pieces of quenched glass observed optically or by SEM display two distinct regions of different bubble size, which are hypothesized to correspond to the quenched liquid phase and the quenched vapor phase (Fig. 2f). The silicate-rich liquid that would have quenched to a porcelaneous spheroid at a lower *T* now appears as highly bubbly, silicate-rich glass, whereas the glass with fewer and larger bubbles, often in the form of intimately welded masses of clear spherules, is interpreted to represent the quenched vapor phase. The clear glass balls protruding from the bubble-poor portion of the glass provide supporting evidence that the glass with fewer bubbles is the quenched vapor phase.

Textural recognition of quenched phases is difficult on the H₂O-rich limb of the solvus when the percentage of liquid decreases beyond a certain amount; this creates our largest source of uncertainty. Experiments that are interpreted to have been inside the miscibility gap show mostly clear glass balls, with only a few small spheroids of porcelaneous glass.

Table 2 Results of subsolidus albite solubility experiments from 1.0 to 1.6 GPa and 650 to 690 °C

Run	P (GPa)	T (°C)	Time (h)	H_2O (mg)	Ab (mg)	Run products	Ab solubility (wt%)
Ab314	1.00	690	11	30.978	2.752	Quenched vapor	> 8.10
*Ab276	1.00	690	88	34.456	3.073	Quenched vapor	> 8.19
*Ab275	1.00	690	90	19.287	1.998	Ab + quenched vapor	< 9.39
Ab74	1.25	650	48	24.990	2.614	Paragonite + quenched vapor	n/a
Ab309	1.25	684	24	27.040	9.465	Quenched vapor	> 25.93
*Ab312	1.25	684	15	24.293	9.448	Quenched vapor	> 28.00
*Ab310	1.25	684	23	18.573	7.961	Ab + quenched vapor	< 30.00
Ab145	1.40	660	96	30.541	11.284	Ab + quenched vapor	< 26.98
Ab188	1.40	650	77	7.456	5.061	Ab + quenched vapor	< 40.43
Ab187	1.40	650	77	7.955	6.742	Ab + quenched vapor	< 45.87
Ab174	1.40	665	112	6.850	3.714	Ab + quenched vapor	< 35.16
Ab161	1.40	660	93	17.453	17.463	Ab + quenched vapor	< 50.01
Ab311	1.40	677	26	24.927	10.262	Quenched vapor	> 29.33
Ab305	1.40	677	31	20.911	9.574	Quenched vapor	> 31.41
*Ab304	1.40	677	17	6.698	3.623	Quenched vapor	> 35.10
*Ab303	1.40	677	17	5.097	3.421	Ab + quenched vapor	< 40.16
Ab199	1.60	665	99	7.533	3.205	Quenched vapor	> 29.84
Ab200	1.60	665	99	4.440	2.372	Quenched vapor	> 34.82
Ab208	1.60	665	29	3.963	2.674	Quenched vapor	> 40.29
*Ab313	1.60	665	51	25.058	18.111	Quenched vapor	> 41.95
*Ab213	1.60	665	22	5.163	4.046	Ab + quenched vapor	< 43.94
Ab212	1.60	665	22	4.170	3.971	Ab + quenched vapor	< 48.78

Solubility reported in weight percent as $\frac{\Delta m_{Ab}}{\Delta m_{Ab} + m_{H_2O}} \times 100$

Uncertainties: average standard error in weighings are 1 μg, pressure and temperature are within 0.03 GPa and 3 °C

Run products: *ab* crystalline albite, *quenched vapor* water with dissolved solutes, glass, ± quench paragonite, ± trace albite

Italicized results previously published in Makhluf et al. (2016)

*Experiments that bracket the invariant point on the water-rich limb of the solvus at each pressure

Fig. 1 Schematic isobaric $T - X_{H_2O}$ sections at two pressures, P_1 which is at a pressure lower than the second critical end point pressure, P_2. For P_1, two fluid phases (liquid and vapor) can coexist, and at P_2, only one fluid phase (supercritical fluid) can exist. Letter designation: *A* dry melting temperature, *B* vapor-saturated solidus, *B'* invariant point where albite solubility measurements were conducted, *C* critical point, *star* critical endpoint
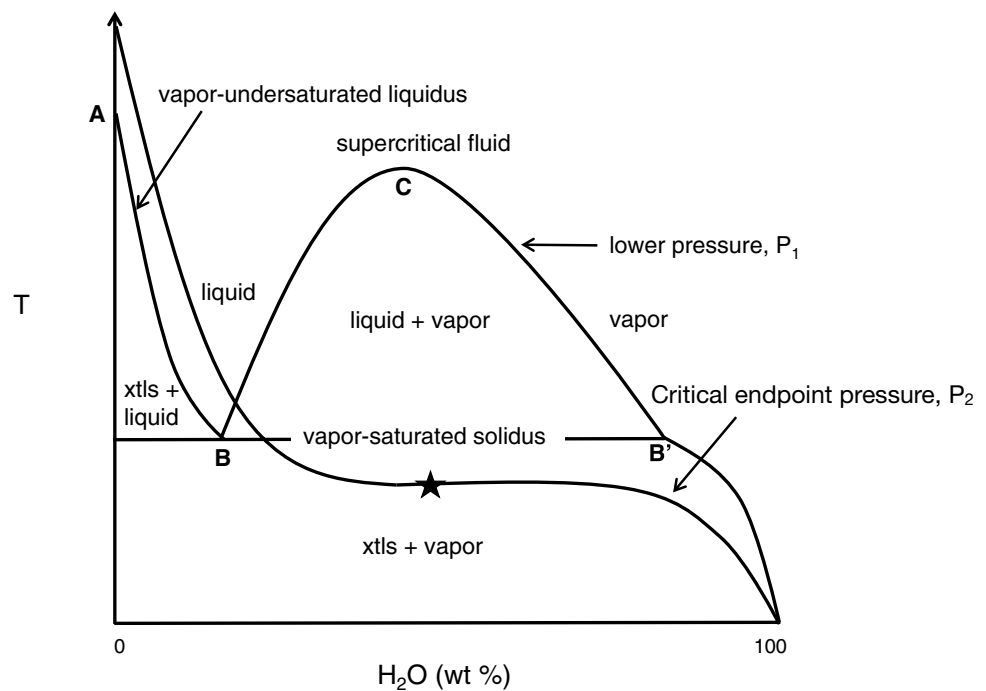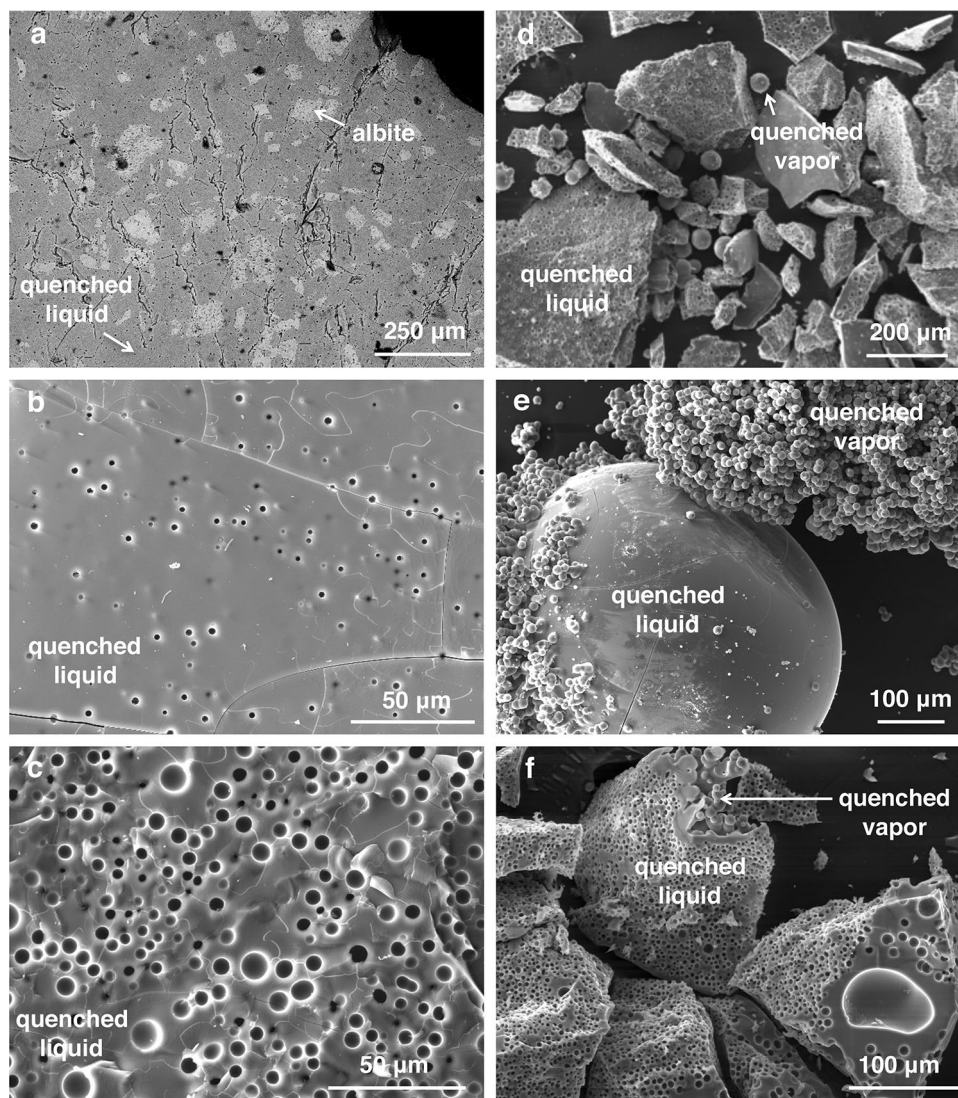
Fig. 2 Secondary electron images of quenched charges. **a** Sample Ab05, 1.0 GPa, 750 °C, 10.93 wt% H_2O, quenched liquid + albite. Recrystallized albite embedded in a hydrous glass, formerly liquid. **b** Sample Ab03, 1.0 GPa, 800 °C, 13.35 wt% H_2O, quenched liquid. Hydrous albitic glass with vapor exsolution bubbles. **c** Sample Ab26, 1.0 GPa, 800 °C, 22.94 wt% H_2O, quenched liquid. Compares to Fig. 3b. Hydrous albitic glass with exsolution bubbles of greater size and abundance. **d** Sample Ab27, 1.0 GPa, 800 °C, 26.13 wt% H_2O, quenched liquid + vapor. Small spheres are the quenched vapor phase and the shards of bubbly glass are the quenched liquid phase. Run Ab26 with slightly less H_2O looked identical, but contained no quenched vapor spheres. **e** Sample Ab35, 1.0 GPa, 900 °C, 74.08 wt% H_2O, quenched liquid + vapor. A porcelaneous patty or spheroid (the silicate-rich liquid phase) is observed in charges quenched from the center of the miscibility gap. The smaller clear balls are interpreted as quench from the coexisting H_2O-rich vapor phase. **f** Sample Ab164, 1.4 GPa, 815 °C, and 49.62 wt% H_2O, quenched liquid + vapor. This sample was at a temperature slightly below the critical temperature. Quenched vapor spheres from the H_2O-rich vapor phase are present as well as bubbly glass from the quenched liquid phase. **g** Sample Ab37, 1.0 GPa, 800 °C, 84.89 wt% H_2O, quenched vapor. Contains both quenched vapor spheres and tiny flakes of hexagonal crystals quenched from the vapor phase. The crystalline quench product is most likely paragonite or hydromica. **h** Sample Ab28, 1.0 GPa, 900 °C, 80.02 wt% H_2O, quenched vapor. Another example of a quenched vapor phase. The quenched vapor phase is a welded mass of balls at these conditions. Desiccation crack pattern occurred during drying. **i** Sample Ab70, 1.0 GPa, 1060 °C, 50.36 wt% H_2O, quenched supercritical fluid. Glass has well-formed exsolution bubbles. **j** Sample Ab165 1.25 GPa, 920 °C, 50.01 wt% H_2O, quenched supercritical fluid. Glass has mostly well-formed exsolution bubbles. **k** Sample Ab133 1.4 GPa, 830 °C, 50.19 wt% H_2O, quenched supercritical fluid. Glass has poorly formed exsolution bubbles. **l** Sample Ab162, 1.7 GPa, 650 °C, 49.97 wt% H_2O, quenched supercritical fluid and albite. Glass has irregularly texture without well-formed exsolution bubbles. Large limpid albite crystal is seen in the top portion of this image. The albite formed in a similar experiment, Ab163, was identified by XRD to be maximally low-structured-state albite
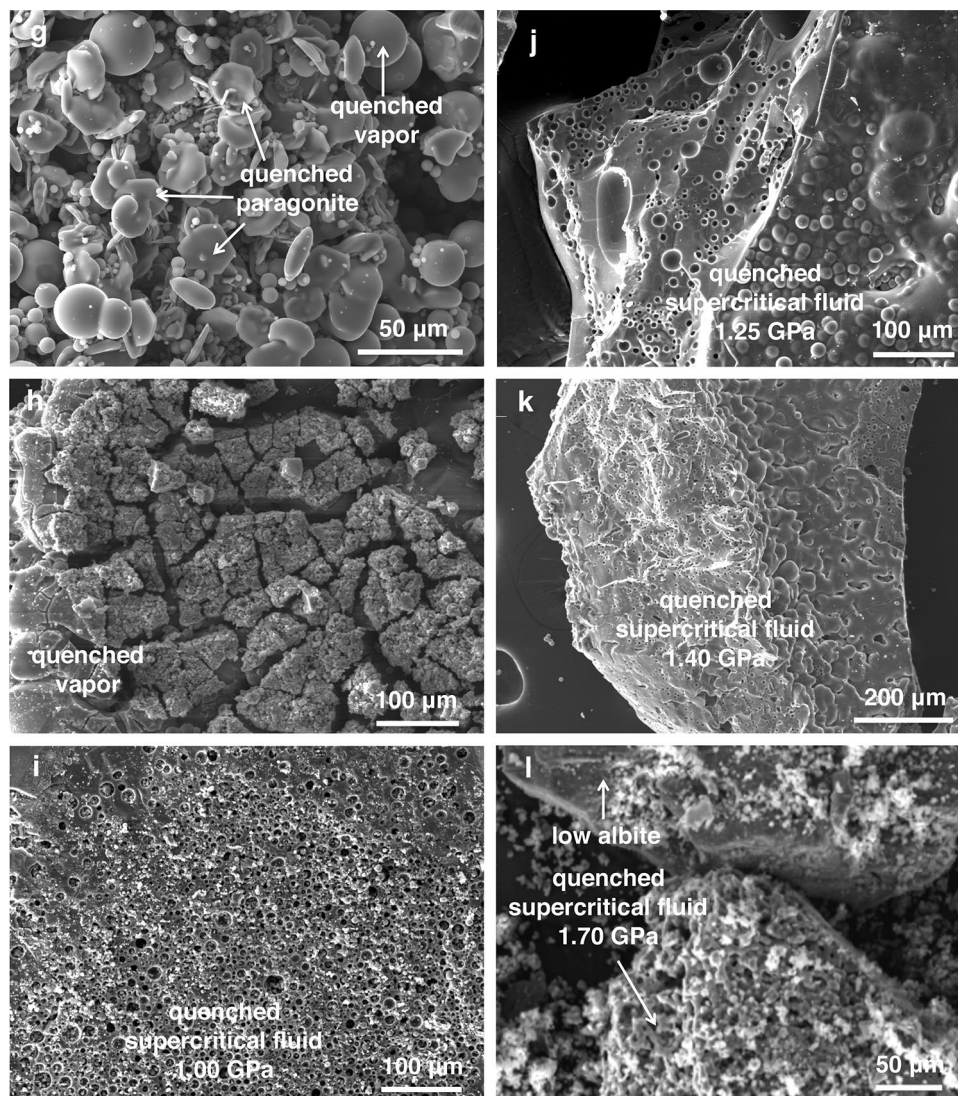
Fig. 2 (continued)

With increasing H_2O, an approximate bracket is located between the miscibility gap and the vapor field by disappearance of the white, opaque, glass spheroids. An additional problem encountered in very H_2O-rich compositions is that a rind of bubble-poor glass on the capsule wall and on the exterior of spheroids can be mistaken for a film of former vapor phase. Our interpretation is that this layer is deficient in bubbles compared with the rest of the quenched melt phase because of short diffusion path lengths to the vapor phase which forms most abundantly in these regions, as documented by Mourtada-Bonnefoi and Laporte (2004). In view of these difficulties in distinguishing quenched vapor from quenched liquid, the near solidus albite solubility measurements become a crucial, quantitative constraint on the H_2O–rich limb of the solvus because of the ambiguity of the quench textures in this region.

Vapor field

At very high water contents, quench products consisting solely of myriad clear glass balls indicate *P–T* conditions within the vapor field (Fig. 2g–h). The glass balls typically contain minute bubbles. Diameters of the glass balls are typically ~ 5–50 μm; larger diameters occur though rarely > 200 μm. The balls are often welded together (Fig. 2h). Small paragonite crystals are seen in Fig. 2g; however, paragonite is not a stable phase at the run conditions for this experiment (800 °C and 1.0 GPa; Goldsmith and Jenkins 1985b) and; therefore, must have formed during quenching.

Supercritical fluid field

The supercritical fluid phase appears at the point in $P - T - X_{H_2O}$ space where the distinction between quenched coexistent fluid phases vanishes. In practice, identification of this field is greatly aided by the context provided by progressive changes in quench texture observed in experiments at subcritical conditions with increasing T while P and composition are held constant. Experiments were conducted at 1.0–1.6 GPa at different temperatures near the crest of the solvus, while holding the H_2O content fixed in the range of ~ 40–60 wt% H_2O. Locating the crest of the solvus by varying the composition proves difficult because of its relatively flat shape and the textural similarity of the quenched coexisting phases. A continuous solubility curve was defined at 1.7 GPa by the lack of an observable miscibility gap.

At the conditions investigated, supercritical fluids quench to vesiculated hydrous glasses and exsolved aqueous fluid charged with particulate and dissolved matter that appears as a milky white oozing fluid upon puncturing of the capsule. Criteria for a quenched supercritical fluid is absence of a porcelaneous glass spheroid and the lack of two regions of distinctly different bubble density in the quenched glass (Fig. 2f). Glass spheroids are seen at temperatures well within the miscibility gap at temperatures ~ 100 °C or more below the critical temperature (e.g. Fig. 2e), whereas glasses with two distinct bubble distributions are seen at temperatures within ~ 100 °C of the critical temperature (e.g. Fig. 2f).

Quenched supercritical fluids show progressive changes in texture with increasing pressure. Figure 2i–k show the progression in quench textures at 50 wt% H_2O with increasing pressure and decreasing temperature. At relatively lower pressures of 1.0–1.25 GPa; Fig. 2i, j), the bubbles in the quenched supercritical fluid are subspherical. A wide range of bubble sizes are interspersed throughout the masses of glasses quenched from supercritical fluids. At 1.4 GPa (Fig. 2k) the quenched supercritical fluid shows irregularly shaped cavities instead of well-formed bubbles. At 1.7 GPa the quenched supercritical fluid quenched to a friable mass (Fig. 2l). Albite was found to be the stable crystalline phase coexisting with supercritical fluid at $T \geq 630$ °C at 1.7 GPa. The subhedral crystals are up to 0.5 mm in the longest dimension (Fig. 2l). Slow XRD scans of albite grown at 650 °C and 1.7 GPa with 50 wt% H_2O (Run Ab162) yielded a value of $\Delta 2\theta_{131\text{-}1\text{-}31}$ of 0.98°, indicating a maximally low structural state (Goldsmith and Jenkins 1985a). We found no evidence for incongruent melting of albite to jadeite and liquid as reported by Boettcher and Wyllie (1969), either microscopically or with XRD.

Albite + vapor field

Charges in the albite + vapor field were identified on the H_2O-rich limb of the solvus at subsolidus temperatures (Goldsmith and Jenkins 1985b) simply by the presence or absence of albite. A series of solubility measurements bracketed the solidus temperature from below using this criterion. Charges in this low-T region resembled those seen in Fig. 2l where run products show recrystallized albite, quenched vapor spheres and micron-size glass shards. Albite solubility was congruent at all conditions investigated except at 1.25 GPa and 650 °C (Run Ab74).

Summary of experimentally constrained phase relations

Figure 3a–e summarize the experimental results in isobaric $T - X_{H_2O}$ binaries. The results at 1.0 GPa include data from Makhluf et al. (2016). The data show that our interpretive scheme based on the quench textures generally gives topologically consistent results. For example, at temperatures between the solidus and closure of the liquid–vapor miscibility gap, the isobaric progression in phase assemblages from low to high water content is $Ab + L \rightarrow L \rightarrow L + V \rightarrow V$. Similarly, consistent phase progression is seen at subsolidus T, and T above the critical point.

The $T - X_{H_2O}$ phase relations (Fig. 3a–d) can be combined with data from Burnham and Jahns (1962) to obtain the solidus temperature (T_{sol}), critical temperatures (T_c), H_2O solubility at the vapor-saturated solidus ($s_{H_2O,vss}$), and albite solubility at the solidus ($s_{Ab,s}$) as functions of pressure:

$$T_{sol}(P) = 995.78 - 833.554P + 772.958P^2 - 238.226P^3 \tag{1}$$

$$T_c(P) = 1078.28 + 352.335P - 368.919P^2 \tag{2}$$

$$s_{H_2O,vss}(P) = 1.35 + 30.720P - 36.428P^2 + 21.205P^3 \tag{3}$$

$$s_{Ab,s}(P) = 0.7806e^{2.6514P}, \tag{4}$$

($R^2 > 0.99$ for Eqs. 1–3, and $R^2 = 0.86$ for Eq. 4), where P is pressure in GPa, T is temperature in degrees centigrade, and s_i is composition in weight percent.

Equation (1) was constrained by bracketing the solidus at 695 ± 5 °C and 1.0 GPa, 692 ± 8 °C and 1.25 GPa, 688.5 ± 11.5 °C and 1.4 GPa, and 667 ± 3 °C and 1.6 GPa, combined with the low-pressure data starting at 0.1 GPa from Burnham and Jahns (1962). Equation (1) is therefore valid at pressures starting from 0.10 to 1.65 GPa.

The critical temperatures used to obtain Eq. (2) were regressed from the critical points as determined from
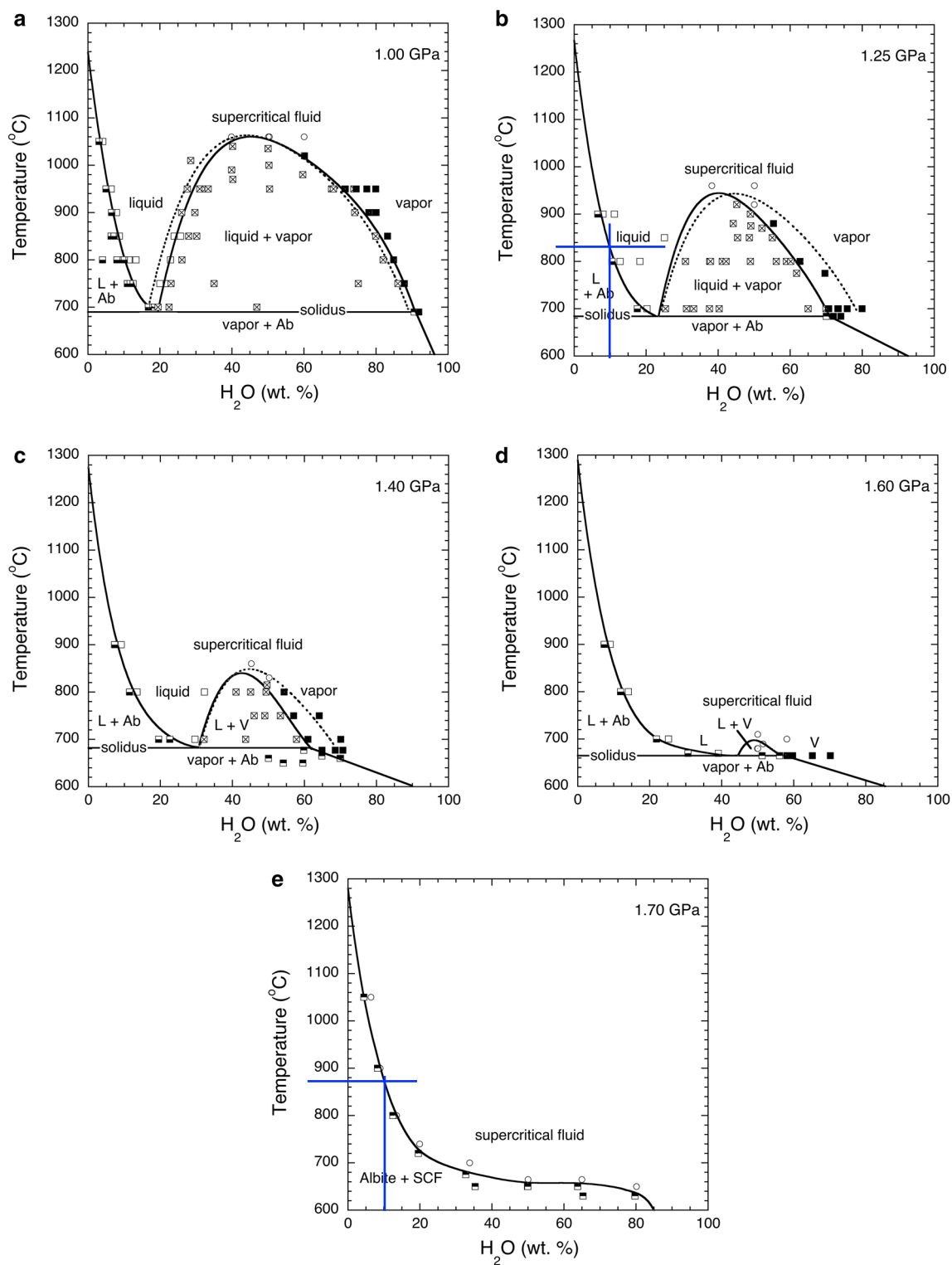
Fig. 3 $T - X_{H_2O}$ binaries for the system NaAlSi$_3$O$_8$–H$_2$O determined by interpretation of textures of quenched charges and solubility measurements. Symbols: bottom half filled squares albite (Ab) + liquid (L), top half filled squares Ab + vapor (V), open squares L, filled squares V, open circles supercritical fluid (SCF), crossed squares L + V, dotted circle SCF or V. **a–d** 1.0, 1.25, 1.4 and 1.6 GPa, respectively. The solvus curves are depicted in three ways: the solid line is a best fit equation through the midpoint brackets, the short-dashed lines are calculated curves from the subregular solution model presented in "Liquid-vapor mixing". **e** 1.7 GPa. The results at this pressure show that albite is stable just below 650 °C at 1.7 GPa. The intersection of the vapor-saturated solidus with the critical curve occurs between 1.6 and 1.7 GPa and at a temperature of 665 ± 10 °C commencing with a stable critical end point

quartic fits to the midpoint brackets of the solvus: 1060 °C at 1.0 GPa, 950 °C at 1.25 GPa, 840 °C at 1.4 GPa, and 700 °C at 1.6 GPa. This equation is valid is calibrated between 1.0 and 1.65 GPa, but can likely be extrapolated down to 0.6 GPa.

The solubility of H_2O in albite liquid along the melting curve (Eq. 3, Fig. 4) was fit using the H_2O contents at the vapor-saturated solidus (18.75 ± 0.73 wt% at 1.0 GPa and 700 °C, 22.82 ± 2.58 wt% at 1.25 GPa and 700 °C, 30.88 ± 1.25 wt% at 1.4 GPa and 700 °C, and 44.5 ± 5.5 wt% at 1.6 GPa and 670–680 °C), combined with the lower pressure data of Burnham and Jahns (1962). Their lower pressure determinations of the H_2O contents at vapor saturation are shown with open diamond symbols in Fig. 4. Equation (3) is valid at pressures between 0.10 and 1.61 GPa which yields H_2O contents up to 44.7 wt% at the critical endpoint.

The solubility of albite in H_2O at near solidus conditions (Eq. 4, Fig. 5) was found to be 8.79 ± 0.60 at 1.0 GPa and 690 °C, 29.00 ± 1.00 at 1.25 GPa and 684 °C, 37.63 ± 2.53 at 1.4 GPa and 677 °C, and 42.95 ± 0.99 at 1.6 GPa and 665 °C. An exponential function was employed to describe this data set in order to obtain physically reasonable results down to lower pressures as well as a near infinite dX/dP slope at the critical endpoint, a thermodynamic requirement for critical mixing of L and V. This equation should only be used between 0.10 and 1.61 GPa.
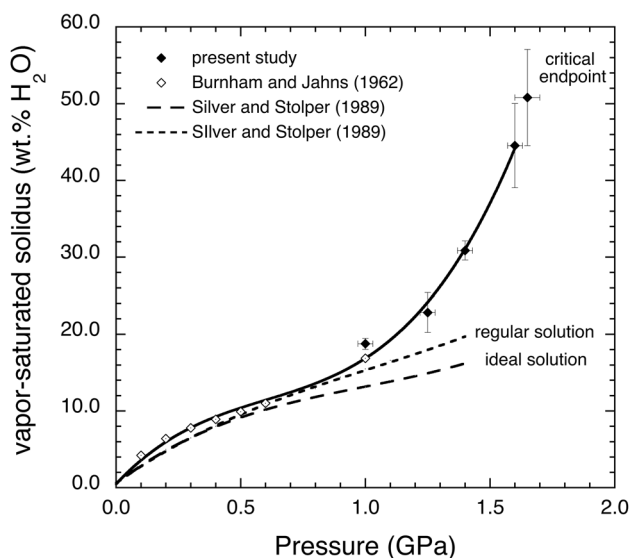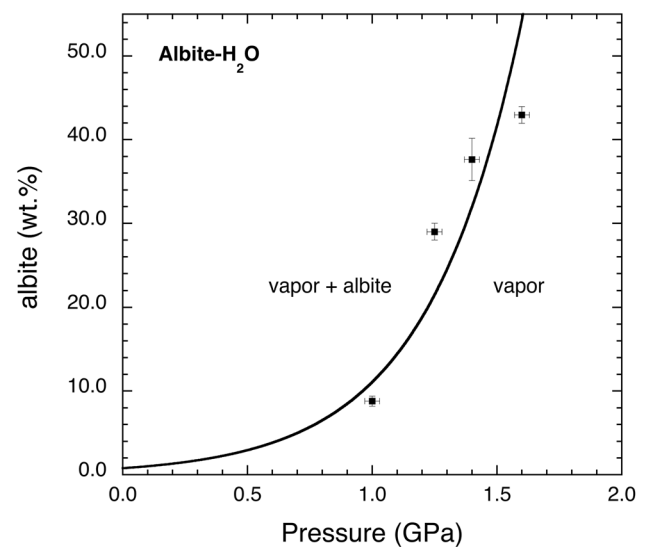

Fig. 5 Albite solubility (wt%) as a function of pressure (GPa). At each pressure, measurements were conducted 5–10 °C below the solidus temperature in order to accurately determine the invariant point on the H_2O-rich limb of the solvus at the solidus. Albite solubility increases from 8.79 ± 0.60 wt% at 1.0 GPa to 42.95 ± 0.99 wt% at 1.6 GPa. An exponential function was used to fit the data because of the thermodynamic requirement of a near infinite dX/dP slope at the critical endpoint, and for physically reasonable results at lower pressures

The critical endpoint temperature and pressure predicted from Eqs. (1) and (2) are 654 °C and 1.65 GPa. The intersection of Eqs. (3) and (4) independently defines the critical endpoint at 1.61 GPa and 44.7 wt% H_2O. Taken together, Eqs. (1–4) constrain the critical endpoint pressure to be in the range of 1.63 ± 0.02 GPa, which agrees with the experiments at 1.7 GPa where we found no evidence for the coexistence of two fluid phases over a large range of compositions and temperatures ranging from 4 to 80 wt% H_2O and 630–1050 °C (Fig. 3e).

Equations (3) and (4) better fit the experimentally determined solvus limb topology than does a single equation with a reasonable number of parameters, and therefore were used as a piecewise function to describe the L and V compositions across the entire binary at any pressure < 1.61 GPa (Fig. 6). A consequence of this approach is that in the vicinity of the critical endpoint composition at approximately 44.7 wt% H_2O, the first derivatives of pressure with respect to composition are nonzero and the second derivatives are not strictly equal, though the derivatives closely approach those values from the left and right of the critical endpoint. These $P–X_{H2O}$ inputs from Eqs. (3) and (4), when combined with the solidus temperatures (Eq. 1), provide the necessary input parameters for rigorous calculation of the Gibbs excess free energy of mixing between H_2O and $NaAlSi_3O_8$ in coexisting liquid and vapor phases.
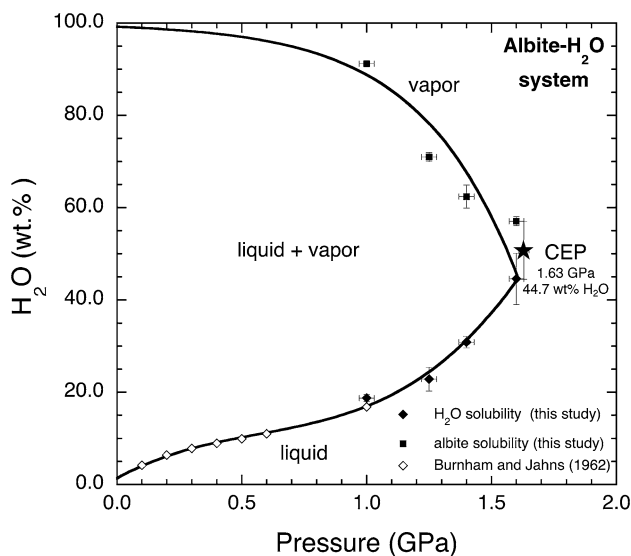

Fig. 4 H_2O content (wt%) at the vapor-saturated solidus as a function of pressure in GPa. The results from Burnham and Jahns (1962; open diamonds) at lower pressure data are an excellent match to the higher-pressure data presented in this study. Our results (filled diamonds) deviate from the Silver and Stolper (1989) regular solution model (dotted line) and their ideal mixing model (dashed line). The near-vertical tangent of the curve near 1.6 GPa signifies a critical end point on the hydrous melting curve of albite at a slightly higher pressure of 1.63 ± 0.02 GPa

Fig. 6 Polythermal phase relations as a function of pressure for liquid–vapor immiscibility in the system $NaAlSi_3O_8$–H_2O at solidus temperatures constructed using Eqs. (3) and (4). The constraints on the critical endpoint (CEP, star symbol) are 1.63 ± 0.02 GPa, 659 ± 5 °C, and ~ 44.7 wt% H_2O. We acknowledge that dX/dP should be infinite at the critical endpoint, however we chose to use a piecewise function for several reasons which are detailed in "Summary of experimentally constrained phase relations". Vapor-saturated solidus H_2O contents are represented with filled diamonds (present study) and open diamonds (Burnham and Jahns 1962); H_2O contents for saturated solutions of dissolved albite in H_2O are represented with filled squares

The deviation between the experimentally determined values and those predicted from Eqs. (3) and (4) can been seen in Fig. 6. The predicted values are in excellent agreement with the experimental values with the exception of the albite solubility measurement at 1.6 GPa. This data point, however, is subject to the most uncertainty given the flatness of the liquidus and solvus near the critical composition.

Discussion

Liquid–vapor mixing

Following Blencoe (1992), we attempted a subregular solution model for the isobaric two-phase envelope and critical points, since all of the two-fluid envelopes determined in this work are somewhat asymmetric. We formulated Margules parameters, W_{H_2O} and W_{Ab}, using the input from Eqs. (1) to (4) and mixing units of 1/8 $NaAlSi_3O_8$ (32.78 g/mol, termed Ab) and H_2O (Knapp and van Vorst 1959; Silver and Stolper 1985).

The Margules parameters at the solidus temperature, or at any T where immiscibility occurs, are determined by setting the chemical potential of Ab equal in coexisting liquid and vapor, and likewise for the chemical potential of H_2O. When the standard states of Ab and H_2O are chosen to be the same in both liquid and vapor phases, then

$$a_{Ab,L} = a_{Ab,V} \tag{5}$$

$$a_{H_2O,L} = a_{H_2O,V}, \tag{6}$$

where the activity of each component at the solidus is given by:

$$\ln a_{Ab,T_{sol}} = \ln X_{Ab,T_{sol}} + \left(1 - X_{Ab,T_{sol}}\right)^2 \\ \left[W_{Ab,T_{sol}} + 2X_{Ab}\left(W_{H_2O,T_{sol}} - W_{Ab,T_{sol}}\right)\right]/RT \tag{7}$$

$$\ln a_{H_2O,T_{sol}} = \ln X_{H_2O,T_{sol}} + \left(1 - X_{H_2O,T_{sol}}\right)^2 \\ \left[W_{H_2O,T_{sol}} + 2X_{H_2O}\left(W_{Ab,sT_{sol}} - W_{H_2O,T_{sol}}\right)\right]/RT, \tag{8}$$

and $X_{Ab,T_{sol}}$ and $X_{H_2O,T_{sol}}$ are mole fraction values consistent with Eqs. (3) and (4). A system of equations can then be solved simultaneously to find $W_{Ab,T_{sol}}$ and $W_{H_2O,T_{sol}}$ at each pressure. The Margules parameters at the critical temperatures can be found by using a constant critical composition of 44.7 wt% H_2O (corresponding to $X_{H_2O,T_c} = 0.595$ and $X_{Ab,T_c} = 0.405$ based on a one-oxygen mole fraction basis), the critical temperatures T_c from Eq. (2) and solving for W_{Ab,T_c} and W_{H_2O,T_c} at each pressure using the equations

$$W_{Ab,T_c} = \frac{RT_c(P)}{6(X_{Ab,T_c}X_{H_2O,T_c})^2}\left(9X_{Ab,T_c}X_{H_2O,T_c} - X_{Ab,T_c} - 1\right) \tag{9}$$

$$W_{H_2O,T_c} = \frac{RT_c(P)}{6(X_{Ab,T_c}X_{H_2O,T_c})^2}\left(9X_{Ab,T_c}X_{H_2O,T_c} - X_{Ab,T_c}X_{H_2O,T_c} - 1\right). \tag{10}$$

It was then assumed that the Margules W parameters vary linearly between the solidus and the critical temperatures according to the following equations:

$$W_{Ab} = W_{Ab,T_c} + \frac{T_c(P) - T}{T_c(P) - T_{sol}(P)}(W_{Ab,T_{sol}} - W_{Ab,T_c}) \tag{11}$$

$$W_{H_2O} = W_{H_2O,T_c} + \frac{T_c(P) - T}{T_c(P) - T_{sol}(P)}(W_{H_2O,T_{sol}} - W_{H_2O,T_c}), \tag{12}$$

where T is in °C. The solvus curves can then be calculated by iteratively solving for the compositions at any given T and P in the range of the 0.6 up to 1.6 GPa. The results of these calculations are plotted as the long-dashed lines outlining the solvus in Fig. 3a–c. For the 1.0 GPa solvus, the deviation between the experiments and the model is within ~ 3 wt% H_2O at all conditions. At 1.25 and 1.4 GPa, the water poor limbs of the solvus are reproduced almost exactly with

deviations less than ~ 2 wt% H_2O, however there is a systematic offset on average of ~ + 5 wt% on the H_2O-rich limbs of the solvus. Because of the proximity of the critical endpoint close to 1.6 GPa, the miscibility gap is vanishingly small not and thus is not included in Fig. 3d.

Comparison with previous work

Schmidt et al. (2014) found that paragonite is a stable phase with liquid at 700 °C and pressures above 1.0 GPa for H_2O-rich compositions on the join $NaAlSi_3O_8$–H_2O (see their Fig. 6). We found paragonite to be a stable phase on this join at 650 °C and 1.25 GPa (Table 2, Run Ab74), where it appeared in abundant thick, felted masses completely replacing albite, similar to textures noted by Manning et al. (2010). However, at the solidus P–T conditions in the present experiments, we found only a very small amount (~ 1% of the charge) of mica in large (~ 50–100 μm across) but thin flakes which we interpret to be a metastable quench phase from the fluid, inasmuch as we found similar flakes in an experiment at 800 °C and 1.25 GPa (Run Ab119, Table 1). Paragonite is not stable even on its own composition at 800 °C and 1.25 GPa (Chatterjee 1970; Holland and Powell 1998). Schmidt et al. (2014) reported metastable paragonite at temperatures up to 771 °C at 1.1 GPa; a true stability region of paragonite on the join $NaAlSi_3O_8$–H_2O awaits experimental definition.

Our critical curve for the system $NaAlSi_3O_8$–H_2O is similar to that of Shen and Keppler (1997), but with substantially smaller uncertainty and with a systematic offset to slightly higher pressures (see Fig. 3.5 B in Manning 2018). The systematic offset of our critical curve to higher pressures closely matches the determination of Schmidt et al. (2014). We found only congruent melting of albite at all conditions, so our results do not support a singular point as proposed by Boettcher and Wyllie (1969), where hydrous albite melting becomes incongruent (i.e. $Ab + V \rightarrow Jd + L$). The reemergence of a two-fluid field in the system $NaAlSi_3O_8$–H_2O at still higher pressures and temperatures (Hayden and Manning 2011) may further complicate the phase relations. However, our data are not at sufficiently high pressures to resolve this feature.

At pressures above 1.4 GPa, our solidus curve departs significantly from that derived from studies using high albite (Boettcher and Wyllie 1969; Bohlen et al. 1982; Eggler and Kadik 1979); however, it corresponds closely with the results of Goldsmith and Jenkins (1985b) on low albite. Our solidus determination is particularly robust because it is constrained by multiple observations. In addition to simple bracketing of the presence or absence of liquid, the trajectories of the liquidus and the left limb of the liquid–vapor solvus, as determined by textural criteria independently confirm the vapor-saturated solidus H_2O content at all pressures. Additionally,

in all cases the invariant points found by extrapolation of the right limb of each solvus to the corresponding solidus temperature are in excellent agreement with the independent determinations of these point using the subsolidus solubility measurements. Contrasting behavior of low and high albite may explain why we observed congruent hydrous melting of albite up to the critical endpoint, in contrast to the observations of Boettcher and Wyllie (1969) at the same P–T conditions. It is also notable that Goldsmith and Jenkins (1985b) observed a marked difference in texture between quench material at ≥ 1.6 GPa and the quenched glass at lower pressures; this is consistent with our interpretation of a near supercritical liquid at the solidus at 1.6 GPa.

The vapor-saturated solidus curve determined between 1.0 and 1.6 GPa (Fig. 4) is a smooth continuation of the accelerating trend to 1.0 GPa observed by Burnham and Jahns (1962), who used essentially the same experimental methods. The solidus temperature versus melt composition curve of Fig. 4 departs significantly from that modeled by Silver and Stolper (1989), whose model intentionally did not incorporate higher P data complicated by the possible onset of critical phenomena.

Spera (1974) used a Margules method similar to the one presented in "Liquid-vapor mixing" and extrapolated experimental melting data for a hydrous fluid-saturated natural pegmatite composition. His prediction of critical mixing of fluid and melt at 2.61 GPa and 700 °C is actually in reasonable agreement with the experimental determination for haplogranite–H_2O by direct observation in an optical diamond–anvil cell by Bureau and Keppler (1999).

P–T projection of phase relations

Figure 7 is a P–T projection of H_2O concentrations in hydrous albite liquids at the liquidus (dashed lines) and at vapor saturation (thin solid lines), as constrained by data in this study and at lower P (< 1.0 GPa) by those of Paillat et al. (1992). The H_2O saturated solidus combines our new data with those of Goldsmith and Jenkins (1985b) and Burnham and Jahns (1962). Liquid compositions are calculated from the subregular reduction of experimental data as described in "Liquid-vapor mixing". Isopleths of H_2O on the liquidus surface are effectively straight lines whose dP/dT slopes increase to coincide with the solidus curve at the critical endpoint. The 30 wt% liquidus isopleth is an interpolation. H_2O contents of vapor-saturated liquids are flat and nearly straight, with minor curvature near the critical curve.

Applications to petrology

Feldspathic liquids are formed in nature by water-undersaturated melting of amphibolites and metasediments in subduction zones. They are the antecedents of the

Fig. 7 $P-T$ projection in the NaAlSi$_3$O$_8$–H$_2$O system plotting liquidus isopleths (dashed lines) with solvus isopleths (thin solid lines). Bounding these isopleths are that of the vapor-saturated solidus and the critical curve which terminates at a critical endpoint pressure of 1.63 ± 0.02 GPa and 659 ± 5 °C. The curves are constrained at lower P–T conditions using the data from Burnham and Jahns (1962), Goldsmith and Jenkins (1985b) and Paillat et al. (1992)
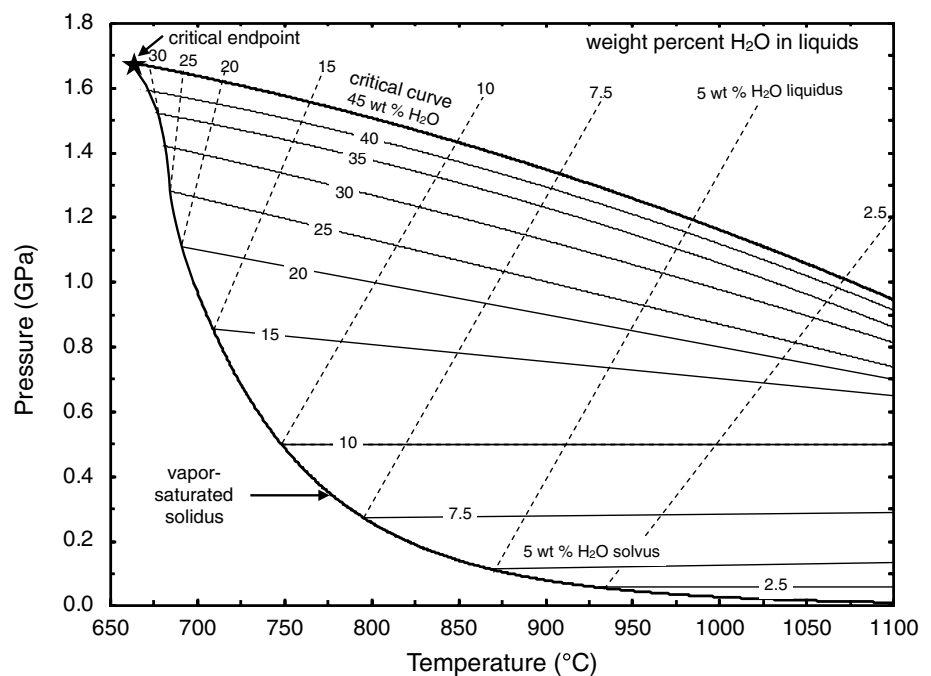
tonalite–trondhjemite–granodiorite (TTG) gneisses and metasediments that are believed to make up much of the deep continental interiors. These magmas may, to a close approximation, be modeled in the simple system NaAlSi$_3$O$_8$ (Ab)–KAlSi$_3$O$_8$ (Or)–SiO$_2$ (Qz)–H$_2$O. Several authors (e.g. Burnham and Jahns 1962) have shown that the four-component system may, in turn, be approximated in many of its phase relations and physical–chemical properties by the two-component subsystem NaAlSi$_3$O$_8$–H$_2$O. Bureau and Keppler (1999) found evidence of a critical curve in the hydrous simple granite system at 1.30–1.69 GPa and 830–1000 °C by optical observation of phase assemblages in an externally heated diamond–anvil cell. Their critical curve for albite–H$_2$O and granite–H$_2$O are quite comparable to that determined in the present study for albite–H$_2$O. Moreover, the vapor-saturated solidus melt coexisting with feldspar and quartz becomes increasingly sodic and SiO$_2$ poor at pressures > 1 GPa (Luth 1976), so that granitic liquids formed by partial hydrous melting of quartzofeldspathic rocks would be close to the subsystem NaAlSi$_3$O$_8$–H$_2$O in composition. For these reasons, this simple subsystem is an attractive model for magma generation at deep crust/subcrust levels.

The H$_2$O contents of vapor-undersaturated melts in equilibrium with albite are substantially higher at a given temperature than in simple granite melts in equilibrium with feldspar and quartz (Makhluf et al. 2017). For instance, at 800 °C and 1.0 GPa, Fig. 7 shows that liquidus NaAlSi$_3$O$_8$–H$_2$O melt contains about 10 wt% H$_2$O, whereas a liquidus granite melt at the same conditions has a maximum of 5.6 wt% H$_2$O. This difference results from the higher Si/alkali ratio of the granitic melt. For melts generated at

very high pressure and lower temperatures in a subduction zone setting, which will be more Na-rich and less SiO$_2$-rich than a normal granite, the H$_2$O contents of liquidus melts may be close to the higher values of albite melts.

An important property of quartz–feldspar–H$_2$O systems at near-critical pressures and temperatures (i.e. where H$_2$O-rich melts and silicate-rich aqueous solutions approach each other in composition and properties) is that fluids generated by mineral dehydration or other processes may acquire indefinitely large amounts of solute silicate components without undergoing a discrete phase change such as melting. Moreover, very silicate-rich solutions (or very H$_2$O-rich melts) become largely depolymerized with pressures above about 1 GPa, with attendant great decrease in viscosity (Audétat and Keppler 2004). The mobility, or ease of penetration into deep-crust/upper mantle rocks of low permeability, of ordinary magmas would be greatly enhanced, while chemical reactions with host rocks would be expected to be quite different from those with either more dilute aqueous fluids or H$_2$O-poor silicate liquids, in that they might combine the metasomatic capability of both kinds of fluids, specifically the ability to transport alkali elements and halogens while retaining significant solubility for Fe, Ti, and the alkaline earth elements, which are relatively insoluble in dominantly aqueous fluids. Our experiments have demonstrated the great fluxing power of near-critical NaAlSi$_3$O$_8$–H$_2$O fluids for feldspar recrystallization by the growth of large crystals of maximally low albite at temperatures as low as 650 °C.

Conditions of $P > 1.0$ GPa and $T < 700$ °C, estimated for recrystallization of the Catalina (California) Schist by Bebout and Barton (1993), would, in the presence of

an aqueous fluid, be near-critical. Although it is probable that deeply subducted sediments and volcanic rocks undergo progressive dehydration reactions and become H_2O deficient, the overwhelming evidence for hydrous alteration, as in the vein complexes of the Catalina Schist of California (Bebout and Barton 1993) undoubtedly requires copious infiltration of H_2O from a deep-seated source; hence our description of the H_2O-rich portion of the albite–H_2O system are pertinent to petrogenesis. The term "migmatites" applied by these authors to the pervasive quartz–feldspar vein complexes which characterize the Catalina Island subduction terrain may be appropriate in its magmatic context in view of the P–T conditions, described in the present paper, under which magmatic and hydrothermal processes in common rocks lose their distinction. We find that albite continues to melt (or dissolve) congruently in the presence of H_2O to pressures immediately adjacent to the high-pressure breakdown of albite to jadeite and quartz, and therefore that the presence of jadeite in high P/T rocks implies either pressures greater than albite breakdown or silica deficiency, even if a H_2O-rich fluid was present. Other examples of supercritical fluids derived from subducted slab sediments have been discussed recently (Ferrando et al. 2005; Hermann et al. 2013; Huang and Xiao 2015; Zheng and Hermann 2014; Zheng et al. 2011).

The possibility also exists that supercritical or near-critical H_2O-rich silicate melts may be of importance in high-temperature reactivation processes in the cratonal, or interior continent environment. Some workers dismiss this possibility on the grounds that the only feasible source of H_2O for melting is thought to be resident in the hydrous mafic minerals, biotite and amphibole (Stevens and Clemens 1993). The maximum amount of H_2O available would not exceed 1 wt%, even for biotite-rich source rocks. However, other authors cite reasons to believe that much larger amounts of H_2O are sometimes present. Wickham and Taylor (1987) and McLelland et al. (2002) consider that large amounts of water of surficial origin could be carried downward to sites of partial melting in continental interiors in thermally driven convection cells. Other sources of H_2O for deep melting could be exsolution from very hydrous basalts intruded into the deep crust (Litvinovsky and Podladchikov 1993; Webster et al. 1999) and brines of various origins (Aranovich et al. 1987, 2013).

If near-supercritical fluids can be generated in interior-continent settings, there may be application to several features commonly observed in granitic bodies and to conjectures regarding the segregation of granitic liquids from sites of melting. These include the apparent ease of segregation (extractability) of deep-crust-generated granitic liquids, the possibility that granitic liquids can be agents of pervasive metasomatism in the deep crust and upper mantle, and the conspicuous localization of granites and migmatites in the middle and upper crust

Several workers have discussed the possibility that H_2O-rich felsic liquids could be an important factor in metasomatic alteration of the deep crust (Alberti and Comin-Chiaramonti 1976; Hasalová et al. 2008) and the ultramafic upper mantle (Pilet et al. 2002; Prouteau et al. 2001). The last two papers point to the fact that felsic liquids would be able to perform certain kinds of metasomatism in the source regions of basaltic magmas, such as depletion in the high field-strength elements Ti and Ta, that would be impossible if the metasomatizing agent were merely an aqueous fluid. Hill (1995) described a deep-crustal shear zone in the New Zealand Fiordland where granitic pegmatites are inferred to have been intruded at 680 °C and 1.2 GPa. Such magmas would be near-critical, especially in view of the possibility of high fluorine, boron or Na contents (Sowerby and Keppler 2002). Sørensen (1983) recorded regional granitization in the deep-seated Nordre Strømfjord shear zone of West Greenland. Under these P–T conditions granitic H_2O-rich fluids would be of very low viscosity, to judge from quench textures in the present experiments, and capable of intimate penetration of country rocks. Hasalová et al. (2008) interpreted quartz–feldspar grain boundary assemblages in high-pressure gneisses from the Czech Republic to infer that massive metasomatism had occurred in these rocks under granulite facies conditions by percolating magmas. If this interpretation is correct, it would imply that the magmas had lower viscosity than currently supposed. Bureau and Keppler (1999) pointed out that rising supercritical silicate–H_2O mixtures must inevitably split into hydrothermal and silicate magma fractions at some level where the expanding solvus in hydrous granitic magmas overwhelms a near-critical fluid, resulting in the sudden increase in the viscosity of the silicate-rich fraction. This could possibly be used to explain the conspicuous localization of migmatite complexes in the middle crust (Olsen et al. 2004).

Conclusions

- Binary phase relations in the $NaAlSi_3O_8$–H_2O system have been established between 1.0 and 1.7 GPa and 630 and 1060 °C by precise measurements of the liquidus H_2O contents, albite solubility, vapor saturation, and interpretations of quench material from liquids, vapors, and supercritical fluids.

- Albite solubility increases substantially from less than 8.79 ± 0.60 wt% at 1.0 GPa, to nearly 42.95 ± 0.99 wt% at 1.6 GPa.

- The H_2O content of liquids at the vapor-saturated solidus increases strongly from 18.75 ± 0.73 wt% at 1.0 GPa to 44.5 ± 5.5 at 1.6 GPa.

- The measurements at the vapor-saturated solidus agree with the lower P measurements of Burnham and Jahns (1962) using the same techniques, but deviate from the models of Silver and Stolper (1989).
- The solubility measurements of both H_2O at the vapor-saturated solidus and the near-solidus albite solubility measurements indicate that there is a critical endpoint in the $NaAlSi_3O_8$–H_2O system between 1.63 ± 0.02 GPa at 659 ± 5 °C and approximately 44.7 wt% H_2O as determined from the intersection of the solidus curve with the critical curve, and the intersection of the vapor-saturated solidus with the exponentially increasing albite solubility measurements at the solids (Eqs. 1–4).
- We constructed a thermodynamic model based on the subregular mixing theory using our measurements and those of previous studies that is applicable across a wide range of pressures from 0.6 GPa, up to the critical endpoint pressure of 1.63 ± 0.02 GPa. The model accurately reproduces the solvus curves while satisfying the data for albite solubility, the vapor-saturated solidus conditions, and the critical conditions.

References

Alberti A, Comin-Chiaramonti P (1976) The metamorphic evolution of Tromöy (arendal area-South Norway). Tschermaks Mineral Petrogr Mitteilungen 23(3):205–220

Aranovich LY, Shmupovich K, Fed'kin V (1987) The H_2O and CO_2 regime in regional metamorphism. Int Geol Rev 29(12):1379–1401

Aranovich L, Newton R, Manning C (2013) Brine-assisted anatexis: experimental melting in the system haplogranite–H_2O–NaCl–KCl at deep-crustal conditions. Earth Planet Sci Lett 374:111–120

Audétat A, Keppler H (2004) Viscosity of fluids in subduction zones. Science 303(5657):513–516

Bartoli O, Acosta-Vigil A, Ferrero S, Cesare B (2016) Granitoid magmas preserved as melt inclusions in high-grade metamorphic rocks. Am Mineral 101(7):1543–1559

Bebout GE, Barton MD (1993) Metasomatism during subduction: products and possible paths in the Catalina Schist, California. Chem Geol 108(1–4):61–92

Behrens H (1995) Determination of water solubilities in high-viscosity melts: an experimental study on $NaAlSi_3O_8$ and $KAlSi_3O_8$ melts. Eur J Mineral 7:905–920

Blencoe JG (1992) A two-parameter Margules method for modelling the thermodynamic mixing properties of albite-water melts. Earth Environ Sci Trans R Soc Edinb 83(1–2):423–428

Boettcher A, Wyllie P (1969) Phase relationships in the system $NaAlSiO_4$–SiO_2–H_2O to 35 kilobars pressure. Am J Sci 267(8):875–909

Bohlen SR, Boettcher A, Wall V (1982) The system albite–H_2O–CO_2: a model for melting and activities of water at high pressures. Am Mineral 67(5–6):451–462

Boyd F, England J (1963) Effect of pressure on the melting of diopside, $CaMgSi_2O_6$, and albite, $NaAlSi_3O_8$, in the range up to 50 kilobars. J Geophys Res 68(1):311–323

Bureau H, Keppler H (1999) Complete miscibility between silicate melts and hydrous fluids in the upper mantle: experimental evidence and geochemical implications. Earth Planet Sci Lett 165(2):187–196

Burnham CW (1975) Water and magmas; a mixing model. Geochim Cosmochim Acta 39(8):1077–1084

Burnham CW, Jahns RH (1962) A method for determining the solubility of water in silicate melts. Am J Sci 260(10):721–745

Chatterjee ND (1970) Synthesis and upper stability of paragonite. Contrib Mineral Petrol 27(3):244–257

Cooper LB, Ruscitto DM, Plank T, Wallace PJ, Syracuse EM, Manning CE (2012) Global variations in H_2O/Ce: 1. Slab surface temperatures beneath volcanic arcs. Geochem Geophys Geosyst 13(3):1–27

Eggler DH, Kadik A (1979) The system $NaAlSi_3O_8$–H_2O–CO_2 to 20 kbar pressure; I, Compositional and thermodynamic relations of liquids and vapors coexisting with albite. Am Mineral 64(9–10):1036–1048

Ferrando S, Frezzotti M, Dallai L, Compagnoni R (2005) Multiphase solid inclusions in UHP rocks (Su-Lu, China): remnants of supercritical silicate-rich aqueous fluids released during continental subduction. Chem Geol 223(1–3):68–81

Gavrilenko M, Krawczynski M, Ruprecht P, Li W, Catalano JG (2019) The quench control of water estimates in convergent margin magmas. Am Mineral 104(7):936–948

Goldsmith JR, Jenkins DM (1985a) The high—low albite relations revealed by reversal of degree of order at high pressures. Am Mineral 70(9–10):911–923

Goldsmith JR, Jenkins DM (1985b) The hydrothermal melting of low and high albite. Am Mineral 70(9–10):924–933

Grove TL, Chatterjee N, Parman SW, Médard E (2006) The influence of H_2O on mantle wedge melting. Earth Planet Sci Lett 249(1–2):74–89

Grove TL, Till CB, Krawczynski MJ (2012) The role of H_2O in subduction zone magmatism. Annu Rev Earth Planet Sci 40:413–439

Hasalová P, Štípská P, Powell R, Schulmann K, Janoušek V, Lexa O (2008) Transforming mylonitic metagranite by open-system interactions during melt flow. J Metamorph Geol 26(1):55–80

Hayden LA, Manning CE (2011) Rutile solubility in supercritical $NaAlSi_3O_8$–H_2O fluids. Chem Geol 284(1–2):74–81

Hermann J, Spandler CJ (2007) Sediment melts at sub-arc depths: an experimental study. J Petrol 49(4):717–740

Hermann J, Spandler C, Hack A, Korsakov AV (2006) Aqueous fluids and hydrous melts in high-pressure and ultra-high pressure rocks: implications for element transfer in subduction zones. Lithos 92(3–4):399–417

Hermann J, Zheng Y-F, Rubatto D (2013) Deep fluids in subducted continental crust. Elements 9(4):281–287

Hill EJ (1995) A deep crustal shear zone exposed in western Fiordland, New Zealand. Tectonics 14(5):1172–1181

Holland T, Powell R (1998) An internally consistent thermodynamic data set for phases of petrological interest. J Metamorph Geol 16(3):309–343

Huang J, Xiao Y (2015) Element mobility in mafic and felsic ultrahigh-pressure metamorphic rocks from the Dabie UHP Orogen, China: insights into supercritical liquids in continental subduction zones. Int Geol Rev 57(9–10):1103–1129

Hunt JD, Manning CE (2012) A thermodynamic model for the system SiO_2–H_2O near the upper critical end point based on quartz solubility experiments at 500–1100 °C and 5–20 kbar. Geochim Cosmochim Acta 86:196–213

Kawamoto T, Kanzaki M, Mibe K, Matsukage KN, Ono S (2012) Separation of supercritical slab-fluids to form aqueous fluid and melt components in subduction zone magmatism. Proc Natl Acad Sci 109(46):18695–18700

Kennedy G, Wasserburg G, Heard H, Newton R (1962) The upper three-phase region in the system SiO$_2$–H$_2$O. Am J Sci 260(7):501–521

Kessel R, Ulmer P, Pettke T, Schmidt M, Thompson A (2005) The water–basalt system at 4 to 6 GPa: phase relations and second critical endpoint in a K-free eclogite at 700 to 1400 °C. Earth Planet Sci Lett 237(3–4):873–892

Knapp W, van Vorst W (1959) Activities and structure of some melts in the system Na$_2$SiO$_3$–Na$_2$Si$_2$O$_5$. J Am Ceram Soc 42(11):559–562

Litvinovsky B, Podladchikov YY (1993) Crustal anatexis during the influx of mantle volatiles. Lithos 30(2):93–107

Luth W (1976) Granite rocks. The evolution of crystalline rocks. Academic Press, New York, pp 333–417

Makhluf A, Newton R, Manning C (2016) Hydrous albite magmas at lower crustal pressure: new results on liquidus H$_2$O content, solubility, and H$_2$O activity in the system NaAlSi$_3$O$_8$–H$_2$O–NaCl at 10 GPa. Contrib Mineral Petrol 171(8–9):75

Makhluf A, Newton R, Manning C (2017) H$_2$O activity in albite melts at deep crustal PT conditions derived from melting experiments in the systems NaAlSi$_3$O$_8$–H$_2$O–CO$_2$ and NaAlSi$_3$O$_8$–H$_2$O–NaCl. Petrology 25(5):449–457

Manning CE (1994) The solubility of quartz in H2O in the lower crust and upper mantle. Geochim Cosmochim Acta 58(22):4831–4839

Manning CE (2018) The influence of pressure on the properties and origins of hydrous silicate melts in Earth's interior. In: Kono Y, Sanloup C (eds) Magmas under pressure: advances in high-pressure experiments on structure and properties of melts. Elsevier, Amsterdam, pp 83–113

Manning CE, Antignano A, Lin HA (2010) Premelting polymerization of crustal and mantle fluids, as indicated by the solubility of albite + paragonite + quartz in H$_2$O at 1 GPa and 350–620 °C. Earth Planet Sci Lett 292:325–336

McLelland J, Morrison J, Selleck B, Cunningham B, Olson C, Schmidt K (2002) Hydrothermal alteration of late-to post-tectonic Lyon Mountain Granitic Gneiss, Adirondack Mountains, New York: origin of quartz–sillimanite segregations, quartz–albite lithologies, and associated Kiruna-type low-Ti Fe-oxide deposits. J Metamorph Geol 20(1):175–190

McMillan PF, Holloway JR (1987) Water solubility in aluminosilicate melts. Contrib Mineral Petrol 97(3):320–332

Mibe K, Kanzaki M, Kawamoto T, Matsukage KN, Fei Y, Ono S (2004) Determination of the second critical end point in silicate-H$_2$O systems using high-pressure and high-temperature X-ray radiography. Geochim Cosmochim Acta 68(24):5189–5195

Mibe K, Kanzaki M, Kawamoto T, Matsukage KN, Fei Y, Ono S (2007) Second critical endpoint in the peridotite–H$_2$O system. J Geophys Res Solid Earth 112(B3):103

Mibe K, Kawamoto T, Matsukage KN, Fei Y, Ono S (2011) Slab melting versus slab dehydration in subduction-zone magmatism. Proc Natl Acad Sci 108(20):8177–8182

Mourtada-Bonnefoi CC, Laporte D (2004) Kinetics of bubble nucleation in a rhyolitic melt: an experimental study of the effect of ascent rate. Earth Planet Sci Lett 218(3–4):521–537

Nakamura Y (1974) The system SiO$_2$–H$_2$O–H$_2$ at 15 kbar. Carnegie Inst Wash Yearb 73:259–263

Newton RC, Manning CE (2008) Thermodynamics of SiO$_2$–H$_2$O fluid near the upper critical end point from quartz solubility measurements at 10 kbar. Earth Planet Sci Lett 274(1–2):241–249

Nowak M, Behrens H (1995) The speciation of water in haplogranitic glasses and melts determined by in situ near-infrared spectroscopy. Geochim Cosmochim Acta 59(16):3445–3450

Olsen SN, Marsh BD, Baumgartner LP (2004) Modelling mid-crustal migmatite terrains as feeder zones for granite plutons: the competing dynamics of melt transfer by bulk versus porous flow. Earth Environ Sci Trans R Soc Edinb 95(1–2):49–58

Paillat O, Elphick SC, Brown WL (1992) The solubility of water in NaAlSi$_3$O$_8$ melts: a re-examination of Ab–H$_2$O phase relationships and critical behaviour at high pressures. Contrib Mineral Petrol 112(4):490–500

Pilet S, Hernandez J, Villemant B (2002) Evidence for high silicic melt circulation and metasomatic events in the mantle beneath alkaline provinces: the Na–Fe–augitic green-core pyroxenes in the Tertiary alkali basalts of the Cantal massif (French Massif Central). Mineral Petrol 76(1–2):39–62

Prouteau G, Scaillet B, Pichavant M, Maury R (2001) Evidence for mantle metasomatism by hydrous silicic melts derived from subducted oceanic crust. Nature 410(6825):197

Schmidt C, Wohlers A, Marquardt K, Watenphul A (2014) Experimental study on the pseudobinary H$_2$O + NaAlSi$_3$O$_8$ at 600–800 °C and 0.3–2.4 GPa. Chem Geol 388:40–47

Shen AH, Keppler H (1997) Direct observation of complete miscibility in the albite–H$_2$O system. Nature 385(6618):710

Silver L, Stolper E (1985) A thermodynamic model for hydrous silicate melts. J Geol 93(2):161–177

Silver L, Stolper E (1989) Water in albitic glasses. J Petrol 30(3):667–709

Sørensen K (1983) Growth and dynamics of the Nordre Strømfjord shear zone. J Geophys Res Solid Earth 88(B4):3419–3437

Sowerby JR, Keppler H (2002) The effect of fluorine, boron and excess sodium on the critical curve in the albite–H$_2$O system. Contrib Mineral Petrol 143(1):32–37

Spera F (1974) A thermodynamic basis for predicting water solubilities in silicate melts and implications for the low velocity zone. Contrib Mineral Petrol 45(3):175–186

Stalder R, Ulmer P, Thompson AB, Günther D (2000) Experimental approach to constrain second critical end points in fluid/silicate systems: near-solidus fluids and melts in the system albite–H$_2$O. Am Mineral 85(1):68–77

Stalder R, Ulmer P, Thompson A, Günther D (2001) High pressure fluids in the system MgO–SiO$_2$–H$_2$O under upper mantle conditions. Contrib Mineral Petrol 140(5):607–618

Stevens G, Clemens J (1993) Fluid-absent melting and the roles of fluids in the lithosphere: a slanted summary? Chem Geol 108(1–4):1–17

Stolper E (1989) Temperature dependence of the speciation of water in rhyolitic melts and glasses. Am Mineral 74(11–12):1247–1257

Till CB, Grove TL, Withers AC (2012) The beginnings of hydrous mantle wedge melting. Contrib Mineral Petrol 163(4):669–688

Truckenbrodt J, Johannes W (1999) H$_2$O loss during piston-cylinder experiments. Am Mineral 84(9):1333–1335

Webster J, Kinzler R, Mathez E (1999) Chloride and water solubility in basalt and andesite melts and implications for magmatic degassing. Geochim Cosmochim Acta 63(5):729–738

Wickham SM, Taylor HP (1987) Stable isotope constraints on the origin and depth of penetration of hydrothermal fluids associated with Hercynian regional metamorphism and crustal anatexis in the Pyrenees. Contrib Mineral Petrol 95(3):255–268

Zeng Q, Nekvasil H (1996) An associated solution model for albite–water melts. Geochim Cosmochim Acta 60(1):59–73

Zheng Y-F, Hermann J (2014) Geochemistry of continental subduction-zone fluids. Earth Planets Space 66(1):93

Zheng Y-F, Xia Q-X, Chen R-X, Gao X-Y (2011) Partial melting, fluid supercriticality and element mobility in ultrahigh-pressure metamorphic rocks during continental collision. Earth Sci Rev 107(3–4):342–374